Novel Energy-Saving Steer-by-Wire System for Articulated Steering Vehicles: A Compact Wheel Loader Case Study

Naseem Daher, Chuang Wang, and Monika Ivantysynova

School of Mechanical Engineering, Purdue University, West Lafayette, Indiana, USA
Email: ndaher@purdue.edu, wang1310@purdue.edu, mivantys@purdue.edu

Abstract

Improving energy efficiency remains a priority in the industrial and academic communities given the ever increasing demand on fossil fuels and their skyrocketing prices. Pump displacement controlled (DC) actuation is an energy efficient alternative to traditional valve controlled actuation. The technology has shown significant fuel savings on mobile machinery when applied to the working hydraulics (implement) functions of such machines. However, DC actuation has never been investigated for use on mobile machinery chassis systems, namely power steering. In this paper and for the first time, a novel closed-circuit pump DC system architecture is devised to perform the power steering system function of a compact wheel loader. A dynamic model of the new system was generated to corroborate concept feasibility, perform system sizing and analysis, and predict performance during standard steering maneuvers. Simulation results showed that a DC power steering system is a feasible, promising, and challenging alternative, which upon further research and development will be brought to life and tested on a prototype machine.

Keywords: displacement control, articulated steering, power steering, dynamic modeling

1 Introduction

Demand for power steering originated from the need for providing assistance to operators in achieving their heading directions, especially as transportation vehicles grew in size and mass. While the main requirements of primitive systems were simply adequate assistance levels and acceptable controllability, today's requirements are more stringent. Given the increased awareness and attention paid to energy efficiency, productivity, and safety, researching alternative technologies is underway. Present-day power steering systems include hydraulic, electric, and electro-hydraulic architectures, which vary based on their energy source, energy transmission, and energy management schemes. Hydraulic power steering is plagued with poor energy efficiency mainly due to throttling losses associated with hydraulic control valves. Electric power steering systems offer better energy efficiency with on-demand power supply and result in improved packaging constraints, but suffer from power limitations at larger vehicle segments. State-of-the-art electrohydraulic steering systems take advantage of the high power density and efficiency of fluid power, but use electronically controlled valves that still suffer from energy inefficiency.

This paper introduces a novel electrohydraulic steer-by-wire steering system and uses a compact wheel loader as a case study. The paper details the high-fidelity co-simulation plant model consisting of a coupled hydraulics and dynamics modules. The new system utilizes a proven energy-saving technology, Displacement Control (DC) developed by Rahmfeld and Ivantysynova (1998), which eliminates hydraulic control valves throttling losses by directly controlling the pump displacement instead.

2 Displacement Control Power Steering

Displacement Control (DC) steering can be classified under electro-hydrostatic power steering, where the steering wheel torque / angle and vehicle speed are sensed and fed back to a controller that adjusts the displacement of a variable displacement pump as opposed to controlling a proportional valve. Figure 1 is provided for identification of components in the proposed circuitry. The actuator (8) velocity is controlled by adjusting the pump (2) speed, displacement, or both. The pump input/output ports are connected to the piston/rod sides of the actuator. The differential fluid flow between the actuator's uneven sides is overcome by means of pilot-operated check valves (6), which keep the low pressure side of the actuator connected to a low pressure source that can either provide or absorb flow to balance the unequal cylinder flow. The low pressure source has its own fixed displacement charge pump (4), driven by the same prime mover (1), providing continuous flow to the cylinder's low pressure side and the pump control system. The low pressure level setting is adjusted via a pressure relief valve (5). An accumulator (not shown) could be used in order to provide high flow rate spikes when sudden high speed cylinder movements are incurred, if the charge pump flow is not sufficient. The system is protected from over-pressurization by means of pressure relief valves (7) installed on both sides of the actuator.

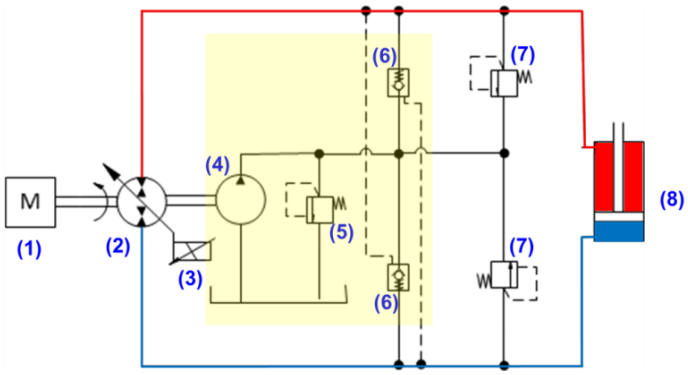

Figure 1: DC Steering Hydraulic Schematic

The pump control system (3), which is detailed in fig. 2, uses a single stage proportional control valve that meters flow to a double rod actuator connected to the pump swash plate. The actuator linear displacement determines the angular position of the swash plate, and therefore the instantaneous pump displacement volume per revolution.

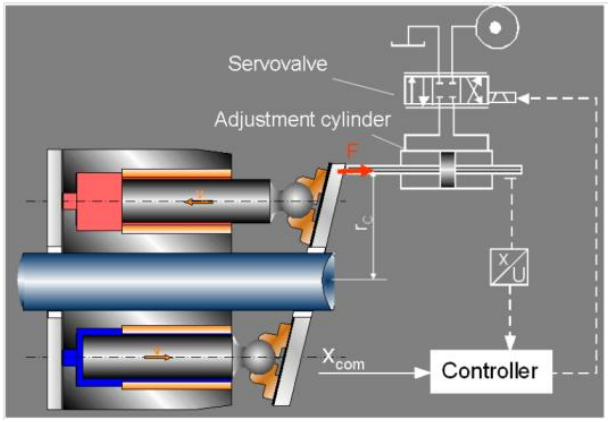

Figure 2: Pump Swash Plate Control System

3 System Modeling

In this section, a detailed dynamic model of the DC steering system plant is described. The system level model is composed of two main building blocks: a hydraulics module and a mechanics one. Figure 3 shows a top-level block diagram of the system model structure and setup. The hydraulics module delivers the required flow rates to induce motion in the linear actuators, which translates into vehicle artiuclation. The pressure levels in the actuator sides are determined by the load computed within the mechanics module mainly due to the opposing loads generated at the ground-tire interface.

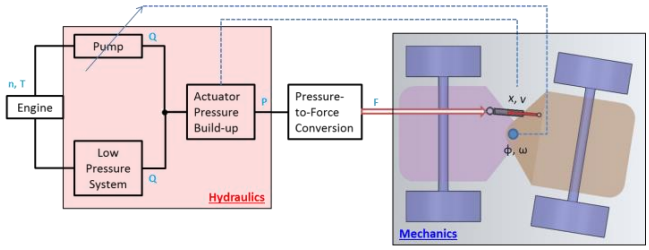

Figure 3: Block Diagram of DC Steering System Model

3.1 Hydraulics Subsystem Model

The hydraulics module includes a variable displacement pump / motor unit modeled with its associated volumetric and torque losses, transmission line losses, a pump control system, a low pressure source system, and a pressure-flow model to determine pressure build-up inside the actuator.

3.1.1 Variable Displacement Pump/Motor Model

The variable displacement axial piston machine is modeled with careful consideration to volumetric and torque losses incurred throughout the entire pump operating range. First, the derived (actual) pump displacement volume is determined using the Toet method. Second, steady-state measurements are recorded at various speeds, displacements, and pressures at constant inlet temperature. The measured data is then fitted to a 3rd degree polynomial to generate the proper loss coefficients as functions of operating conditions. Following are the governing equations that were used to generate the pump model, provided in *pumping* mode operation.

$$Q_e = \beta V_d \, n - Q_s \tag{1}$$

where Q_e is the effective pump flow rate, β is the normalized pump swash plate angle, V_d is the derived pump displacement volume, n is the pump speed, and Q_s is the volumetric loss flow rate given by eq. (2).

$$Q_s\left(V_d, n, \Delta p\right)_{T=const.} = \sum_{i_1=0}^{I_1}\sum_{i_2=0}^{I_2}\sum_{i_3=0}^{I_3} K_Q\left(i_1, i_2, i_3\right).V_d^{i_1}.n^{i_2}.\Delta p^{i_3} \tag{2}$$

The pump effective torque, T_e, is given by eq. (3):

$$T_e = \beta V_d \, \Delta p + T_s \tag{3}$$

where Δp is the pressure differential across the pump ports, and T_s is the torque loss given by eq. (4).

$$T_s\left(V_d, n, \Delta p\right)_{T=cst} = \sum_{i_1=0}^{I_1}\sum_{i_2=0}^{I_2}\sum_{i_3=0}^{I_3} K_T\left(i_1, i_2, i_3\right).V_d^{i_1}.n^{i_2}.\Delta p^{i_3} \tag{4}$$

The derived pump displacement volume obtained via the Toet method is given in eq. (5).

$$V_d = \frac{1}{n}.\frac{\sum_{j=1}^{k} Q_{ej}.\sum_{j=1}^{k}\Delta p_j^2 - \sum_{j=1}^{k}\Delta p_j.\sum_{j=1}^{k}\Delta p_j Q_{ej}}{k.\sum_{j=1}^{k}\Delta p_j^2 - \left(\sum_{j=1}^{k}\Delta p_j\right)^2} \tag{5}$$

3.1.2 Pressure-Flow Equations

The pressure build-up inside the actuator chambers is determined from the conservation of mass principle, which leads to the pressure being a function of the sum of flow

rates entering / leaving the chambers multiplied by the reciprocal of the control volumes hydraulic capacitance. In the following equations, the zero-position is assumed to be at mid-stroke, and the actuator displacement / velocity are positive during the compression stroke (fig. 4).

$$p_A = \frac{1}{C_{HA}} \int \left(Q_A + A_A . \dot{x} - Q_{Li} - Q_r \right) dt \qquad (6)$$

where p_A is the piston (A) side pressure, C_{HA} is control volume A hydraulic capacitance, Q_A is the net flow entering the piston chamber, A_A is the piston side area, $\dot{x}$ is the actuator velocity, Q_{Li} is the internal leakage flow across the actuator chambers, and Q_r is the relief valve flow rate.

$$C_{HA} = \frac{1}{K} \left\{ \left(\frac{H}{2} - x \right) A_A + V_{dead} + V_{LA} \right\} \qquad (7)$$

Where K is the fluid bulk modulus, H is the total actuator stroke, x is the actuator position, V_{dead} is the dead volume inside the actuator, and V_{LA} is the transmission line A volume.

Similarly, the pressure on side B (rod) is determined via eq. (8) and eq. (9).

$$p_B = \frac{1}{C_{HB}} \int \left(-Q_B - A_B . \dot{x} + Q_{Li} - Q_r \right) dt \qquad (8)$$

$$C_{HB} = \frac{1}{K} \left\{ \left(\frac{H}{2} + x \right) A_B + V_{dead} + V_{LB} \right\} \qquad (9)$$

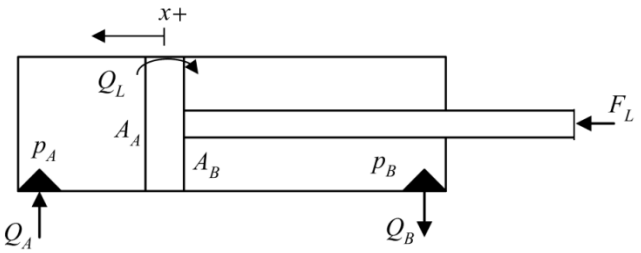

Figure 4: Actuator Pressure-Flow Diagram

3.1.3 Actuator Friction Model

The sliding friction behavior between the actuator's rod and cylinder housing is modeled based on the Stribeck curve regime, which accounts for static friction, coulomb friction, and viscous friction effects.

$$F_R(\dot{x}) = d_v \dot{x} + sign(\dot{x}) \left(F_C + F_H e^{\frac{-|\dot{x}|}{\tau_H}} \right) \qquad (10)$$

where F_R is the resultant friction force, d_v is the viscous friction coefficient, F_C is the Coulomb friction force, F_H is the static friction force, and τ_H is the static friction force constant. A sample plot of the actuator friction force is shown in fig. 5.

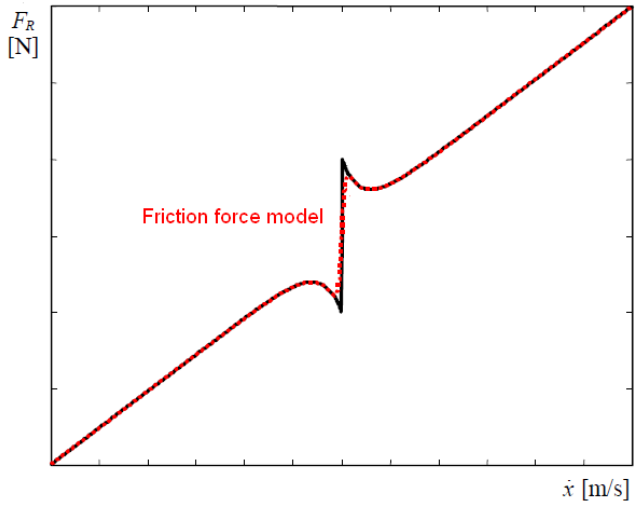

Figure 5: Actuator Stribeck Friction Curve

3.1.4 Transmission Line Losses

Transmission line losses are derived from the Navier-Stokes equations by balancing the pressure forces against the viscous forces. Given that the lines configuration and fluid viscosity are virtually constant, the pressure drop in the transmission lines, Δp_L, could be determined by multiplying the effective flow rate by a constant gain per eq. (11).

$$\Delta p_L = \frac{8 \mu l_L \nu}{R_L^2} = \left[\frac{8 \mu l_L}{A_L . R_L^2} \right] . Q_e \qquad (11)$$

where μ is the fluid dynamic viscosity, ν is the fluid kinematic viscosity, and l_L, R_L,and A_L are the transmission line length, radius, and area respectively.

3.1.5 Low Pressure System

The low pressure system consists of a fixed positive displacement charge pump, two pressure relief valves, and two pilot-operated check valves (POCV) shown in fig. 6.

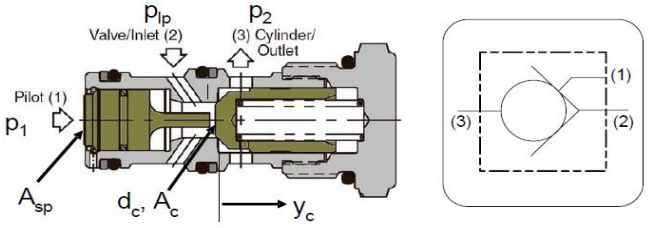

Figure 6: Pilot-Operated Check Valve

The POCV is modeled using a force balance on the pilot spool, which determines both its displacement, y_c, as well as the mode of operation i.e. normal flow versus reverse flow.

Normal Flow Direction:

$$y_c = \frac{1}{k_0} \left[A_c (p_{LP} - p_2) - F_{k0} \right] \qquad (12)$$

Reverse Flow Direction:

$$y_c = \frac{1}{k_0}\left[A_{sp}(p_1 - p_{LP}) + A_c(p_{LP} - p_2) - F_{k0}\right] \quad (13)$$

The resulting POCV flow is given by eq. (14).

$$Q_c = \alpha_D \sqrt{\pi A_c}\, 2 y_c\, sign(\Delta p) \sqrt{\frac{2}{\rho}|\Delta p|} \quad (14)$$

$$\Delta p = p_{1/2} - p_{LP} \quad (15)$$

where A_c is the cone orifice area, p_{LP} is the pressurized low pressure, p_1 is the pilot pressure, p_2 is the cylinder / outlet pressure, F_{K0} is the spring pre-load force, k_0 is the spring rate, A_{sp} is the spool area, and α_D is the discharge coefficient.

3.1.6 Pump Control System

The dynamics of the pump control system responsible for adjusting the swash plate angle are dominated by the servovalve dynamics, which are modeled as a linear second order transfer function from the commanded input voltage signal, u_{SV}, to the output spool position, y_{SV}, per eq. (16).

$$\frac{Y_{SV}(s)}{U_{SV}(s)} = \frac{\omega_{SV}^2}{s^2 + 2\zeta_{SV}\omega_{SV}s + \omega_{SV}^2} \quad (16)$$

where ω_{SV} is the servovalve natural frequency and ζ_{SV} is the valve's damping ratio.

3.2 Mechanics Module

Two separate mechanics modules were generated to allow for performing simulations of two types of common wheel loader maneuvers. The first model is a 1-DOF model where the loader articulates while stationary, simulating a truck loading cycle where the load is transferred from one side to the other. The second model is a 3-DOF model where the loader articulates as it travels, simulating transferring a load at a work site.

3.2.1 1-DOF Dynamic Model

The wheel loader was modeled as two sub-frames connected in the center at the articulation (revolute) joint. For simplicity, the rear sub-frame was fixed to the ground and only the front sub-frame was allowed to rotate, resulting in 1-DOF motion. The linear actuator was modeled as two rigid bodies, rod and cylinder, moving relative to one another along an axial (prismatic) joint. The hydraulic force acts on the rod causing it to translate inside the cylinder, which induces rotational motion of the sub-frame about the articulation (revolute) joint. The rotational motion is a result of the balance of moments about the articulation joint (fig. 7) given in eq. (17).

$$F_{str} * r_j - N_f . \mu_{tf} . \frac{wb}{2} - (d_{AJ} + d_{Tire\_Lat}).\omega_f = I_f \dot{\omega}_f \quad (17)$$

where F_{str} is the steering force, r_j is the normal distance between the articulation joint and the steering actuator force line of action, N_f is the front axle normal load, wb is the vehicle wheelbase, μ_{tf} is the friction coefficient between the tire and the ground, d_{AJ} is the articulation joint damping coefficient, d_{Tire_Lat} is the tires lateral damping coefficient, ω_f is the front sub-frame articulation angle rate, and I_f is the front sub-frame moment of inertia.

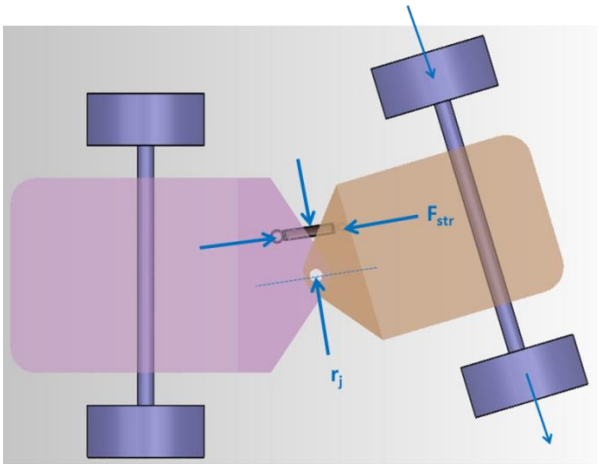

Figure 7: 1-DOF Dynamic Model

3.2.2 3-DOF Dynamic Model

The 1-DOF model only allows for simulating static steering maneuvers. In order to simulate a moving vehicle, a multi-DOF model is then required. However, making changes to the steering system of any moving vehicle requires a deep understanding of the vehicle dynamics aspect. The mechanics module primarily consists of a 3-DOF vehicle dynamics model based on the Lagrangian equation. The Lagrangian approach was adopted due to the complexity of forces and constraints associated with articulated vehicles, where the Newtonian approach is strenuous to apply given the vectorial nature and continuous variation of the forces and accelerations at hand.

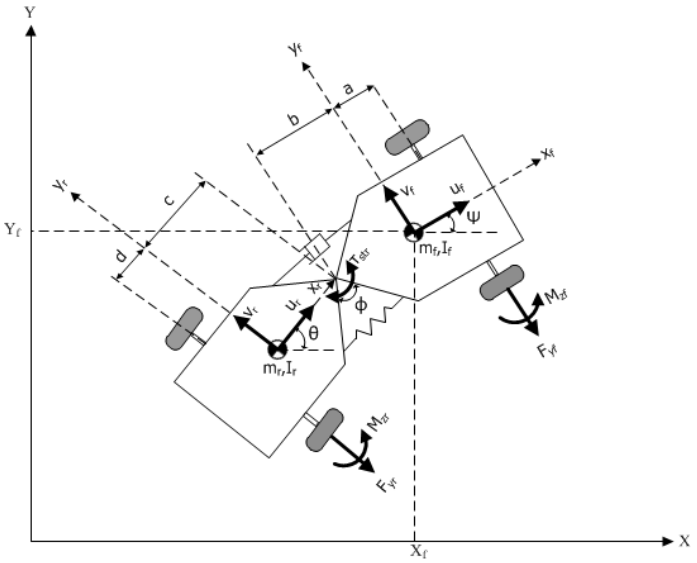

Figure 8: Articulated Vehicle Dynamics

The standard form of the Lagrange equation is given in eq. (18) below:

$$\frac{d}{dt}\left(\frac{\partial L}{\partial \dot{q}_i}\right)-\frac{\partial L}{\partial q_i}+\frac{\partial D}{\partial \dot{q}_i}=Q_i \tag{18}$$

where L is the Lagrangian function (defined as kinetic energy, T, minus potential energy, V), q is the set of generalized coordinates, D is the dissipative function, and Q_i is the set of generalized forces and moments. The kinetic energy includes the translational and rotational motions of two constrained sub-frames as shown in eq. (19). The potential energy and dissipative function are functions of the (equivalent) torsional spring and damping constants, and the articulation angle / rate as shown in eq. (20) and eq. (22).

$$\begin{aligned} T=&\frac{1}{2}m_f(\dot{X}_f^2+\dot{Y}_f^2)+\frac{1}{2}I_f\dot{\psi}^2+\ldots \\ &\frac{1}{2}m_r(\dot{X}_r^2+\dot{Y}_r^2)+\frac{1}{2}I_r\dot{\theta}^2 \end{aligned} \tag{19}$$

$$V=\frac{1}{2}K_{aj}(\psi-\theta)^2 \tag{20}$$

$$L=T-V \tag{21}$$

$$D=\frac{1}{2}C_{aj}(\dot{\psi}-\dot{\theta})^2 \tag{22}$$

Given the constraint imposed by the articulation joint, the rear sub-frame motion can be expressed in terms of the front sub-frame motion, yielding the modified kinetic energy expression given by eq. (23).

$$\begin{aligned} T=&\frac{1}{2}m_f(\dot{X}_f^2+\dot{Y}_f^2)+\frac{1}{2}I_f\dot{\psi}^2+\ldots \\ &\frac{1}{2}m_r[(\dot{X}_f+b\sin\psi\,\dot{\psi}+c\sin\theta\,\dot{\theta})^2+\ldots \\ &(\dot{Y}_f-b\cos\psi\,\dot{\psi}-c\cos\theta\,\dot{\theta})]^2+\frac{1}{2}I_r\dot{\theta}^2 \end{aligned} \tag{23}$$

The originally selected set of generalized coordinates, q, consisted of the global X and Y coordinates, and the angles, ψ and θ, which the front and rear sub-frames make relative to the global X abscissa, respectively. However, to allow for performing maneuvers with large deviations from the global axes such as steady-state cornering, and to reduce the order of the system, a coordinate transformation to the local front sub-frame longitudinal and lateral velocities, u_f and v_f respectively, is necessary per eq. (24) and eq. (25).

$$u_f=\dot{X}_f\cos\psi+\dot{Y}_f\sin\psi \tag{24}$$

$$v_f=-\dot{X}_f\sin\psi+\dot{Y}_f\cos\psi \tag{25}$$

As a result the Lagrangian equations of the X and Y coordinates are replaced with those of u_f and v_f respectively.

$$\frac{d}{dt}\frac{\partial T}{\partial u_f}-\frac{\partial T}{\partial v_f}\dot{\psi}=Q_{u_f} \tag{26}$$

$$\frac{d}{dt}\frac{\partial T}{\partial v_f}+\frac{\partial T}{\partial u_f}\dot{\psi}=Q_{v_f} \tag{27}$$

Another substitution that simplifies the system of equations as well as allows for explicitly stating the articulation angle, ϕ (a desired state variable), is to apply eq. (28).

$$\phi=\psi-\theta \tag{28}$$

Consequently, the following set of coordinates was selected:

$$\mathbf{q}(t)=\left(u_f,v_f,\psi,\dot{\phi}\right)^T \tag{29}$$

where $\dot{\psi}$ is the front yaw angle rate, and $\dot{\phi}$ is the articulation angle rate.

Next, the rear sub-frame local velocities are expressed in terms of the front sub-frame local velocities assuming small articulation angle approximation.

$$u_r=u_f-v_f\phi+b\phi\dot{\psi} \tag{30}$$

$$v_r=u_f\phi+v_f-(b+c)\dot{\psi}+c\dot{\phi} \tag{31}$$

At last, the kinetic energy is now expressed in terms of the desired generalized coordinates, u_f, v_f, ψ, and ϕ as shown in eq. (32).

$$\begin{aligned} T=&\frac{1}{2}m_f\left(u_f{}^2+v_f{}^2\right)+\frac{1}{2}I_f\dot{\psi}^2+\frac{1}{2}m_r[u_f{}^2+v_f{}^2\phi^2\ldots \\ &+b^2\phi^2\dot{\psi}^2-2u_fv_f\phi+2bu_f\phi\dot{\psi}-2bv_f\phi^2\dot{\psi}+u_f^2\phi^2\ldots \\ &+v_f^2+(b+c)^2\dot{\psi}^2+2u_fv_f\phi-2u_f\phi(b+c)\dot{\psi}\ldots \\ &-2v_f(b+c)\dot{\psi}+c^2\dot{\phi}^2+2u_fc\phi\dot{\phi}+2v_fc\dot{\phi}\ldots \\ &-2c(b+c)\dot{\phi}\dot{\psi}]+\frac{1}{2}I_r\dot{\psi}^2-I_r\dot{\psi}\dot{\phi}+\frac{1}{2}I_r\dot{\phi}^2 \end{aligned} \tag{32}$$

Using the virtual work principle, the right hand sides of the Lagrangian equations are resolved. Referring to fig. 8, the following virtual work equation is arrived at.

$$\begin{aligned} \delta W=&\delta_{y_f}\left(F_{y_f}+F_{y_r}\right)+\ldots \\ &\delta\psi[aF_{y_f}-(b+c+d)F_{yr}+M_{zf}+M_{zr}]+\ldots \\ &\delta\phi[(c+d)F_{yr}-M_{zr}] \end{aligned} \tag{33}$$

For determining the tire lateral forces, it is first necessary to determine the tire lateral slip angles. The tire lateral slip angle is defined as the angle between the actual traveling direction of the tire and the direction of the tire centerline. Using small angle approximation, the average slip angles of the front and rear tires are given by eq. (34) and eq. (35).

$$\alpha_f = \frac{v_f + a\dot{\psi}}{u_f} \tag{34}$$

$$\alpha_r = \frac{v_f - (b+c+d)\dot{\psi} + (c+d)\dot{\phi}}{u_f} + \phi \tag{35}$$

For this paper, the linear tire model is used given its simplicity, linear property, and applicability for the maneuvers under consideration relative to speed, articulation angle, and such. The linear tire model is given by eq. (36) through eq. (39).

$$F_{y_f} = -N_f C_{\alpha_f} \alpha_f \tag{36}$$

$$F_{y_r} = -N_r C_{\alpha_r} \alpha_r \tag{37}$$

$$M_{zf} = N_f C_{M\alpha f} \alpha_f = N_f C_{M\alpha f} \left(\frac{v_f + a\dot{\psi}}{u_f} \right) \tag{38}$$

$$M_{zr} = N_r C_{M\alpha r} \left(\frac{v_f - (b+c+d)\dot{\psi} + (c+d)\dot{\phi}}{u_f} + \phi \right) \tag{39}$$

where F_{yf} and F_{yr} are the front and rear tire lateral forces respectively, N_f and N_r are the front and rear axle vertical loads respectively, and $C_{\alpha f}$ and $C_{\alpha r}$ are the front and rear tires lateral force coefficients respectively. M_{zf} and M_{zr} are the front and rear tire aligning moments respectively, and $C_{M\alpha f}$ and $C_{M\alpha r}$ are the front and rear tire aligning moment coefficients respectively. The tire normal loads are determined based on equilibrium analysis of forces and moments leading to the expression of the tire normal forces in terms of the defined vehicle parameters shown in fig. 8.

$$N_f = \frac{m_r g d + m_f g (b+c+d)}{a+b+c+d} \tag{40}$$

$$N_r = \frac{m_f g a + m_r g (a+b+c)}{a+b+c+d} \tag{41}$$

EOM for Generalized coordinate v_f :

The EOM for v_f is obtained after taking time derivatives, partial derivatives, ignoring nonlinear and second order terms, and substituting the generalized force, Q_{vf}, in the Lagrange equation.

$$\begin{aligned} &(m_f + m_r)\dot{v}_f + (-bm_r - cm_r)\ddot{\psi} + (m_f + m_r)u_f\dot{\psi} + (cm_r)\ddot{\phi} = \\ &\left(\frac{-N_f C_{\alpha f} - N_r C_{\alpha r}}{u_f} \right) . v_f - \left(\frac{N_r C_{\alpha r}(c+d)}{u_f} \right)\dot{\phi} - (N_r C_{\alpha r})\phi \ldots \\ &+ \left(\frac{-aN_f C_{\alpha f} - (b+c+d)N_r C_{\alpha r}}{u_f} - (m_f + m_r)u_f \right)\dot{\psi} \end{aligned} \tag{42}$$

The EOM for the remaining two generalized coordinates are obtained in a similar fashion and are listed below in eq. (43) and eq. (44) for completeness.

EOM for Generalized coordinate $\dot{\psi}$:

$$\begin{aligned} &\dot{v}_f\left[-m_r(b+c)\right] + \ddot{\psi}\left[I_f + I_r + m_r(b+c)^2\right] \\ &+ \ddot{\phi}\left(-m_r bc - m_r c^2 - I_r\right) - \dot{\psi}\left[m_r(b+c)u_f\right] \quad = \\ &v_f\left[\frac{-aN_f C_{\alpha f} + (b+c+d)N_r C_{\alpha r} + N_f C_{M\alpha f} + N_r C_{M\alpha r}}{u_f}\right] \ldots \\ &+ \dot{\psi}\left[\frac{\begin{pmatrix} -a^2 N_f C_{\alpha f} - (b+c+d)^2 N_r C_{\alpha r} \\ +aN_f C_{M\alpha f} - (b+c+d)N_r C_{M\alpha r} \end{pmatrix}}{u_f} + m_r(b+c)u_f\right] \ldots \\ &+ \dot{\phi}\left[\frac{(b+c+d)(c+d)N_r C_{\alpha r} + (c+d)N_r C_{M\alpha r}}{u_f}\right] \ldots \\ &+ \phi\left[(b+c+d)N_r C_{\alpha r} + N_r C_{M\alpha r}\right] \end{aligned} \tag{43}$$

EOM for Generalized coordinate $\dot{\phi}$:

$$\begin{aligned} &\dot{v}_f(m_r c) + \ddot{\psi}\left(-m_r c^2 - m_r bc - I_r\right) \\ &+ \ddot{\phi}\left(m_r c^2 + I_r\right) \quad = \\ &v_f\left[\frac{-(c+d)N_r C_{\alpha r} - N_r C_{M\alpha r}}{u_f}\right] + \ldots \\ &\dot{\psi}\left[\frac{(c+d)(b+c+d)N_r C_{\alpha r} + N_r C_{M\alpha r}(b+c+d)}{u_f}\right] + \ldots \\ &\dot{\phi}\left[\frac{-(c+d)^2 N_r C_{\alpha r} - N_r C_{Mr}(c+d)}{u_f} - m_r c u_f\dot{\phi} - C_a\right] + \ldots \\ &\phi\left[-N_r C_{\alpha r} - N_r C_{M\alpha r}\right] \end{aligned} \tag{44}$$

At this point, the equations of motion are expressed in a manner such that the derivatives of the selected generalized coordinates are on the left hand side, whereas the generalized coordinates themselves are on the right hand side of the equations. This format is in accordance with a system of linear first order differential equations. Such formulation lends itself to expressing the system in state space format, which is currently under development for generating a linear model to be used for designing a controller based on modern control theory.

3.3 MSC Adams Model

The compact wheel loader under investigation is designated as the baseline test vehicle to be used for model validation, hardware implementation, and controller development. The

generated models in this paper were developed based on the parameters of the baseline vehicle shown in tab. 1.

Parameter	Description	Value	Unit
m	Vehicle Mass	4100	kg
m_f	Front Sub-frame Mass	1640	kg
m_r	Rear Sub-frame Mass	2460	kg
I_f	Front Sub-frame Moment of Inertia	1500	kg.m^2
I_r	Rear Sub-frame Moment of Inertia	2500	kg.m^2
wb	Vehicle Wheelbase	2.12	m
a	Distance Between Front Sub-frame CG and Front Axle	0	m
b	Distance Between Front CG and Articulation Joint	1.06	m
c	Distance Between Rear CG and Articulation Joint	1.06	m
d	Distance Between Rear Sub-frame CG and Front Axle	0	m
r_j	Normal Distance Between the Articulation Joint and the Steering Actuator Force Line of Action	0.2	m

Table 1: Baseline Wheel Loader Parameters

A multi-body dynamics model was generated in MSC Adams software for two purposes. First, it allows for performing accurate simulations of dynamic steering maneuvers when coupled with the hydraulic subsystem. Second, it will provide a platform for validating the derived linear model, which will be used for advancing the research forward relative to control algorithms development. The model's topology comprises two rigid bodies connected at the articulation joint via a revolute joint. When no articulation angle input is present i.e. no flow to/from the actuator and ignoring leakage across the actuator sides, the hydraulic fluid inside the steering actuator creates the effect of a (stiff) torsional spring at the joint, whose stiffness, K_{aj}, is approximated via eq. (45), which results from the pressure-flow equation.

$$K_{aj} = \frac{K}{V_t} A_A^2 \left(1+\alpha^2\right) \gamma r_j \qquad (45)$$

where K is the fluid bulk modulus, V_t is the total volume of fluid under compression including actuator chambers and transmission lines, A_A is the actuator piston area, α is the area ratio between the actuator sides, γ is a linear conversion factor between the steering actuator linear motion and the vehicle rotational motion, and r_j is the normal distance between the articulation joint and the steering actuator force line of action. As for damping, the articulation joint friction along with the tires lateral damping play the role of a torsional damper present at the joint. This parameter was estimated based on literature review [1] due to lack of measurements at the present time. The PAC 2002 Magic-Formula tire model was selected, which is suitable for the considered maneuvers involving single-lane change and steady-state cornering. Figure 9 shows the generated Adams model that was used during the simulation run.

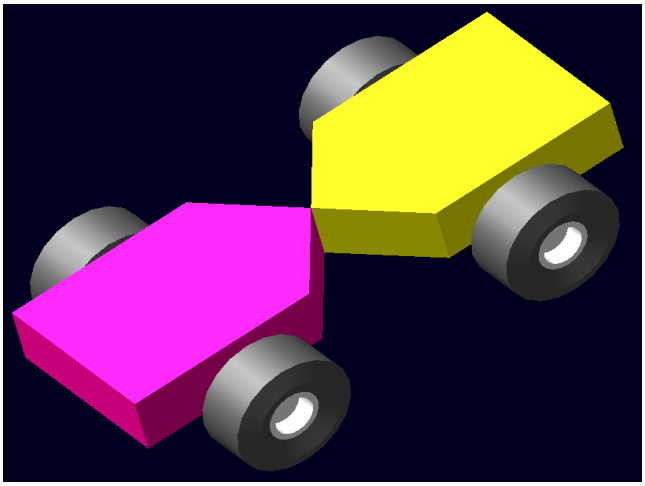

Figure 9: Adams Model of an Articulated Vehicle

3.4 MATLAB Simulink SimMechanics™ Model

A 1-DOF dynamic model was designed in MATLAB Simulink SimMechanics™ environment. The main purpose of the model is to generate a load that the hydraulic subsystem must overcome to induce articulation while the vehicle performs static maneuvers i.e. zero forward speed.

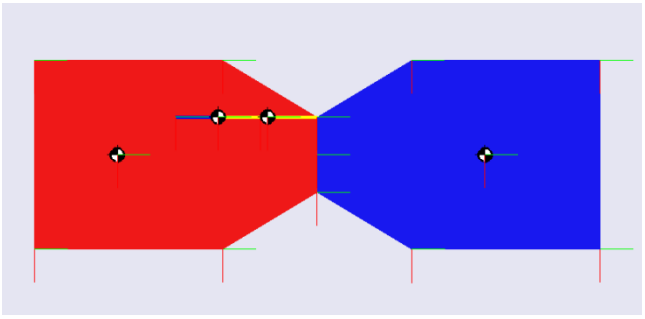

Figure 10: MATLAB Simulink SimMechanics™ Model

4 System Model

Inducing an articulation angle requires a steering torque to be exerted about the articulation joint. This requires coupling the hydraulics and mechanics models. For the Adams model to accept steering force as an input, the

steering actuator was modeled as a linear spring / damper element connected to both subframes (fig. 11).

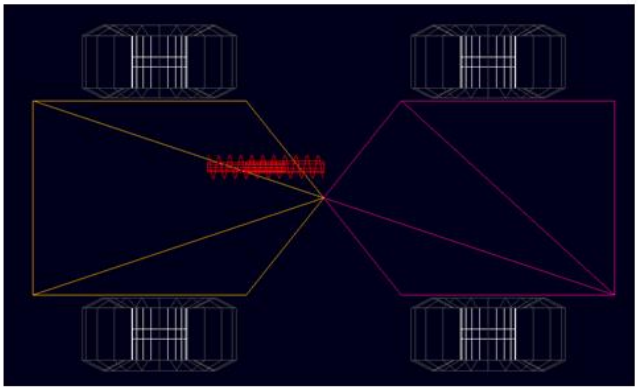

Figure 11: Adams Model Linear Actuator Setup

The Adams plant model was then exported to Simulink in a manner that inputs actuator force and outputs the articulation angle and rate as shown in fig. 12.

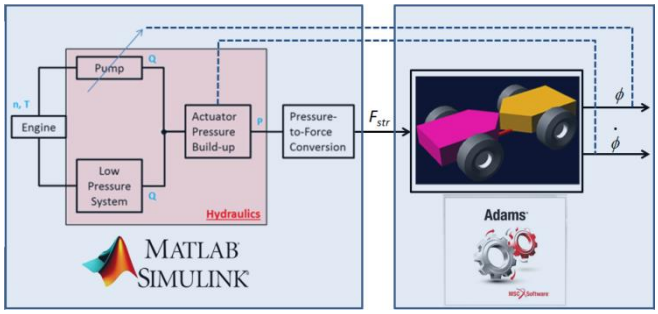

Figure 12: Exported Adams Plant Model into Simulink®

5 Simulation Results

Two maneuvers were simulated: a static maneuver where the vehicle speed is set to zero and the articulation angle is varied between +25° and -25° emulating a static loading cycle; second, a dynamic maneuver where the vehicle forward speed is set to 20 km/hr and the vehicle direction changes between ±9° mimicking a lane change maneuver. The maneuvers were realized via a simple proportional controller providing closed-loop position control. The relevant parameters used during the simulation are given in tab. 2.

Description	**Value**	**Unit**
Pump Displacement Volume	18	cm^3/rev
Engine/Pump Speed	1500	rev/min
Actuator Piston Diameter	0.078	m
Actuator Rod Diameter	0.032	m
Fluid Bulk Modulus	1.9e9	N/m^2
Fluid Density	870	Kg/m^3
Low Pressure System Pressure	25	Bar
Articulation Joint Damping	350	N.m.s/rad

Table 2: Simulation Parameters

5.1 Static Maneuver

Figure 13 shows the vehicle articulation angle varying between +25° and -25°. The ramp-up and ramp-down rates confirm the sizing of the DC steering pump, which was sized to meet the same cycle requirements as the baseline hydrostatic steering system.

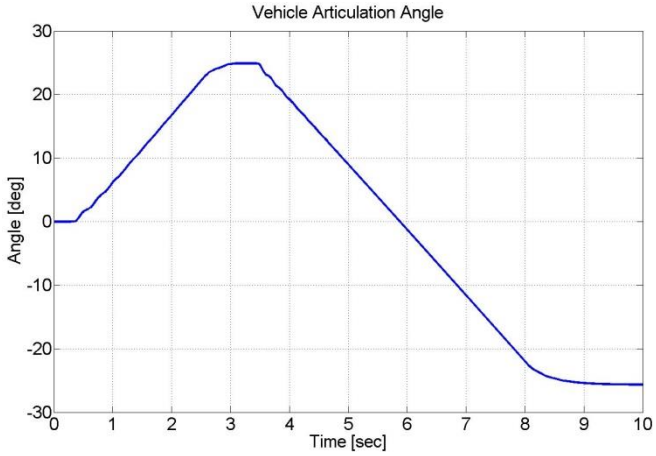

Figure 13: Static Maneuver – Articulation Angle

Figure 14 shows the pressure rise inside the corresponding chambers of the steering actuator. The results serve multiple validation checks. First, given that the steering actuator is mounted with its piston side (A) towards the rear of the vehicle, articulating the vehicle to the left (positive angle) requires the pressure on the rod side (B) to rise and vice versa. Second, the model accurately predicts that higher pressure is needed to articulate the vehicle left than right, since side B has a smaller area than side A. Lastly, the low pressure system successfully kept the low pressure side at the specified setting of 25bar, which confirms the sizing as well as validates the intricate modeling of the low pressure system.

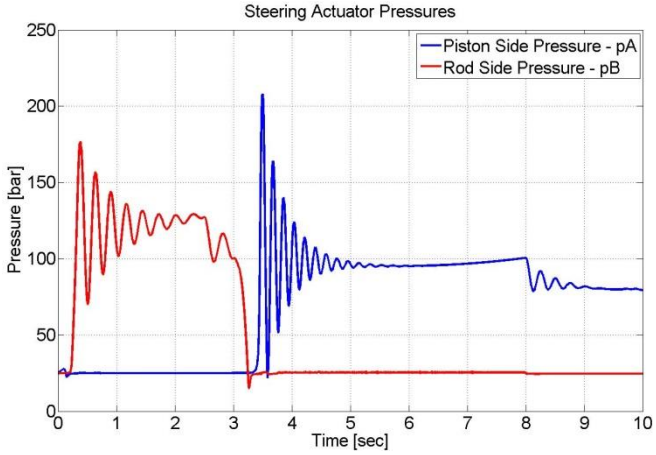

Figure 14: Static Maneuver – Actuator Pressure

Figure 15 shows the net steering actuator force resulting from the pressure differential across the actuator sides.

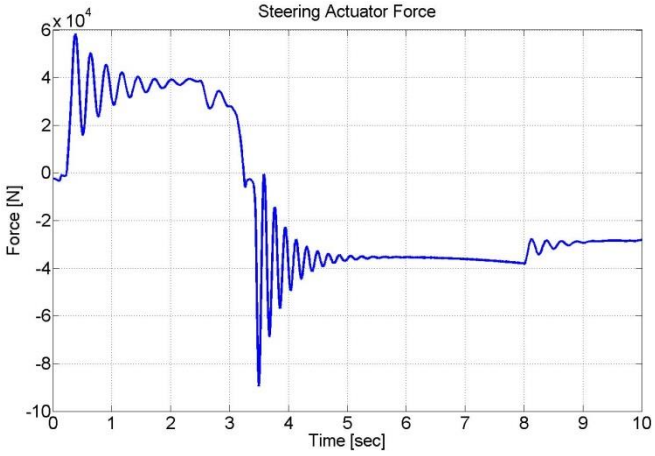

Figure 15: Static Maneuver – Steering Actuator Force

5.2 Dynamic Maneuver

Figure 16 shows the articulation angle of the vehicle during the dynamic maneuver. The vehicle executed a lane change maneuver by changing direction in both ways while driving at 20 km/hr.

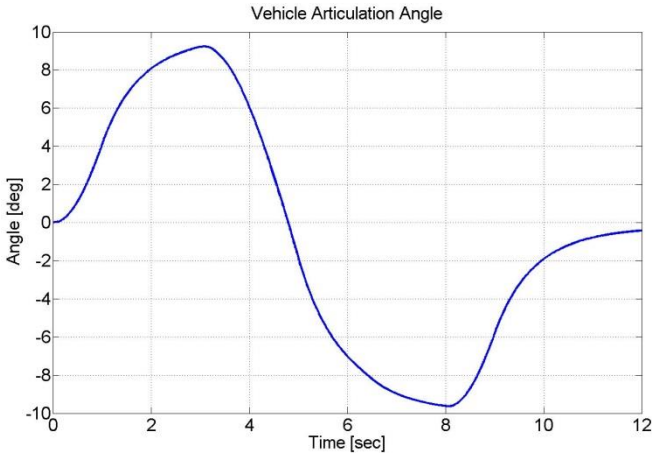

Figure 16: Dynamic Maneuver – Articulation Angle

Figure 17 shows the pressures inside the actuator chambers as the vehicle articulates. Similar results were obtained as in the static maneuver. Articulating the vehicle to the left (positive) requires the pressure on the rod side (B) to rise and vice versa, higher pressure levels are needed to articulate the vehicle left than right since side B has a smaller area than side A, and the low pressure system kept the low pressure side at the specified setting of 25bar.

Figure 18 shows the corresponding steering actuator force resulting from the pressure differential across the actuator chambers. Smaller force magnitudes are observed since the friction coefficient between the tire and ground is lower in dynamic conditions than static ones. When the vehicle reaches the commanded position, the force magnitude returns to zero since no further steering effort is required.

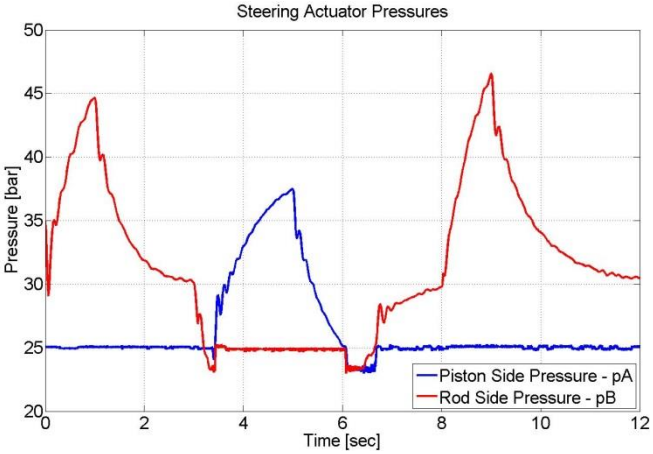

Figure 17: Dynamic Maneuver – Actuator Pressures

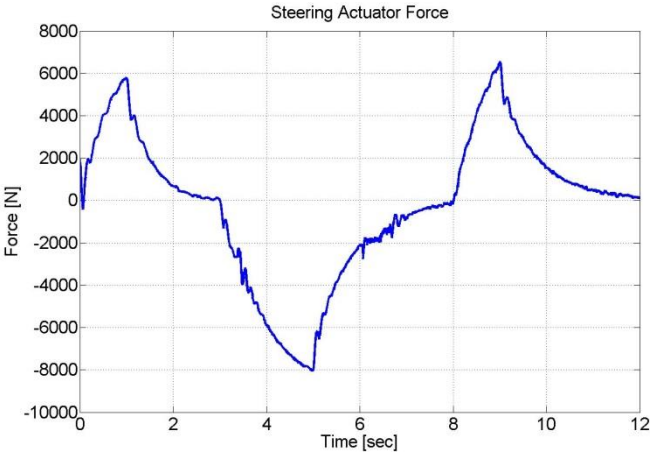

Figure 18: Dynamic Maneuver – Actuator Force

Figure 19 shows the tire lateral slip angles as the vehicle direction deviates from straight-line forward motion. The sign and magnitude of both axles accurately reflect the maneuver at hand, which were verified against manually performed calculations based on eq. (34) and eq. (35). The fact that the slip angles of the tires on the same axle almost overlap, which allows for modeling the vehicle as a bicycle and combining both tires into one.

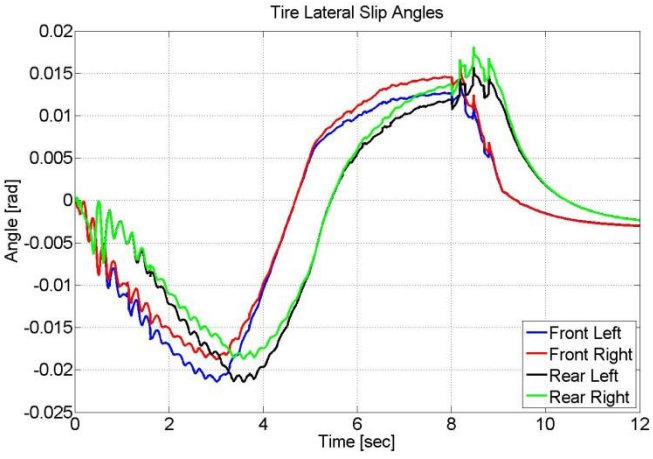

Figure 19: Dynamic Maneuver – Tire Lateral Slip Angles

Figure 20 shows the tire lateral forces resulting from the slip angles shown in fig. 19, the tire normal loads, and the surface type. The sign and magnitude of the tire forces match the theoretical values as computed from eq. (36) and eq. (37).

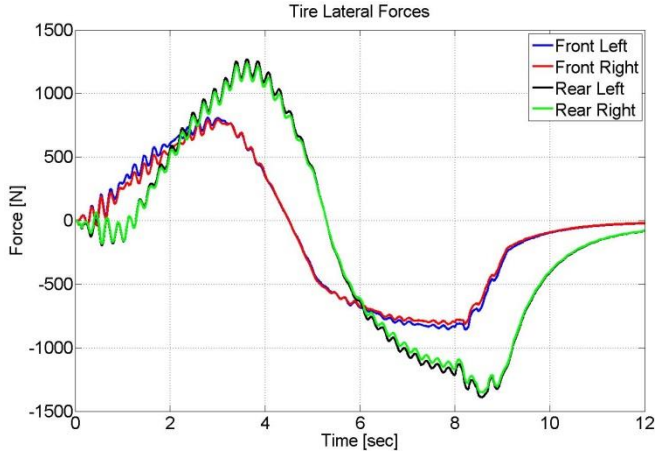

Figure 20: Dynamic Maneuver – Tire Lateral Forces

6 Future Work

The results obtained in this paper will be used to aid in both the derivation process as well as the validation process of linearized models for the hydraulic subsystem, the dynamic subsystem, and the entire system. Linear models allow for exploiting modern control theory techniques pertaining to linear time-invariant (LTI) systems. After designing a controller, the generated control algorithms and dynamic models will be validated and fine-tuned based on measurement results obtained from a baseline test vehicle. This requires retrofitting the test vehicle with a renovated steering column assembly, tactile feedback device, a DC axial piston pump, sensors, actuators, electronics, and a real-time controller.

7 Conclusion

A novel electro-hydraulic steer-by-wire system realized via DC technology has been proposed. High fidelity nonlinear dynamic models of the two subsystems that are at the heart of the new system, hydraulics and mechanics, were developed and validated. Finally, a sophisticated nonlinear system plant model is now available on hand, which will be used for validating the linearized models under investigation, paving the road in front of the design and development of a robust steer-by-wire system controller.

The technology will be demonstrated on a compact wheel loader. Baseline measurements of the stock loader have been conducted, and will be used to compare against the new measurement results after the implementation of the new steering system.

Nomenclature

Q_e	Pump Effective Flow Rate
β	Pump Swash Plate Angle (Normalized)
V_d	Pump Displacement Volume (Derived)
n	Pump Speed
Q_s	Pump/Motor Volumetric Loss
T_e	Pump/Motor Effective Torque
T_s	Pump/Motor Torque Loss
Δp	Pressure Differential Across Pump/Motor Ports
K_Q	Pump/Motor Volumetric Loss Coefficient
K_T	Pump/Motor Torque Loss Coefficient
p	Pressure
Q	Flow Rate
C_H	Hydraulic Capacitance
$\dot{x}$	Actuator Velocity
A	Area
V	Volume
α	Actuator Area Ratio
K_{Li}	Coefficient of Internal Leakage of Actuator
K	Fluid Bulk Modulus
H	Maximum Actuator Stroke (End-to-End)
x	Actuator Position
V_{dead}	Actuator Dead Volume
μ	Fluid Dynamic Viscosity
v	Fluid Kinematic Viscosity
ρ	Fluid Density
F_R	Resultant Friction Force
F_C	Coulomb Friction Force
F_H	Static Friction Force
τ_H	Static Friction Force Constant
l_L	Transmission Line Length
R_L	Transmission Line Radius
y_c	Pilot-Operated Check Valve Spool Displacement
Q_c	Pilot-Operated Check Valve Flow Rate
α_D	Pilot-Operated Check Valve Discharge Coefficient
d_c	Pilot-Operated Check Valve Cone Diameter
y_c	Pilot-Operated Check Valve Cone Position
A_c	Pilot-Operated Check Valve Cone Orifice Area

p_{LP}	Pressurized Low Pressure
p_1	Pilot-Operated Check Valve Pilot Pressure
p_2	Pilot-Operated Check Valve Cylinder / Outlet Pressure
F_{K0}	Pilot-Operated Check Valve Spring Pre-load Force
K_0	Pilot-Operated Check Valve Spring Rate
A_{sp}	Pilot-Operated Check Valve Spool Area
ω_{SV}	Servovalve Natural Frequency
ζ_{SV}	Servovalve Damping Ratio
F_{str}	Steering Actuator Force
r_j	Normal Distance Between the Articulation Joint and the Steering Actuator Force Line of Action
C_{aj}	Articulated Joint Torsional Damping Coefficient
N_f	Front Axle Normal Load
μ_{tf}	Friction Coefficient Between the Tire and Ground
wb	Vehicle Wheelbase
d_{aj}	Articulation Joint Damping Coefficient
d_{Tire_Lat}	Tires Lateral Damping Coefficient
ω_f	Front Sub-frame Articulation Angle Rate
L	Lagrangian Function
T	Kinetic Energy
V	Potential Energy
D	Dissipative Function
Q_i	Generalized Forces
m_f	Front Sub-frame Mass
m_r	Rear Sub-frame Mass
X_f	Front Sub-frame Global Abscissa
Y_f	Front Sub-frame Global Ordinate
x_f	Front Sub-frame Local Abscissa
y_f	Front Sub-frame Local Ordinate
I_f	Front Sub-frame Moment of Inertia
I_r	Rear Sub-frame Moment of Inertia
ψ	Front Sub-frame Yaw Angle
θ	Rear Sub-frame Yaw Angle
ϕ	Articulation Angle
a	Distance between Front C.G. and Front Axle
b	Distance between Front C.G. and Articulation Joint
c	Distance between Rear C.G. and Articulation Joint
d	Distance between Rear C.G. and Rear Axle
K_{aj}	Articulation Joint Equivalent Torsional Stiffness
C_{aj}	Articulation Joint Equivalent Torsional Damping
u_f	Front Sub-frame Longitudinal Velocity
v_f	Front Sub-frame Lateral Velocity
Fy	Tire Lateral Force
M_Z	Tire Aligning Moment
α_s	Tire Slip Angle
α_f	Front Tires Slip Angle
α_r	Rear Tires Slip Angle
N	Axle Normal Load
C_α	Tires Lateral Force Coefficient
$C_{M\alpha}$	Tires Aligning Moment Coefficient
g	Gravity Constant
γ	Conversion Factor Between Actuator Linear Motion and Vehicle Articulation Motion
C_d	Actuator Viscous Damping Coefficient
m_r	Actuator Rod Mass
F_L	Actuator Load Force
DC	Displacement Control
POCV	Pilot-Operated Check Valve
DOF	Degree(s) of Freedom
CG	Center of Gravity
EOM	Equation(s) of Motion

References

[1] Azad, N. Dynamic Modelling and Stability Controller Development for Articulated Steer Vehicles. *Ph.D. dissertation, University of Waterloo*. Waterloo, Ontario, Canada. 2006.

[2] Chen, C. and Tomizuka, M. Modeling and Control of Articulated Vehicles. *Report number UCB-ITS-PRR-97-42, California Partners for Advanced Transit and Highways, Institute of Transportation Studies*, Berkeley, California. 1997.

[3] Crolla D. Automotive Engineering: Powertrain, Chassis System and Vehicle Body. Elsevier Science & Technology Books. Burlington, MA. 2009.

[4] Daher, N. and Ivantysynova, M. Electro-hydraulic energy-saving power steering systems of the future.

Proceedings of the 7th FPNI PhD Symposium, Reggio Emilia, Italy, pp. 929 – 952. 2012.

[5] Greenwood, D. *Principles of Dynamics*. Prentice-Hall, Inc., Englewood Cliffs, New Jersey. 1988.

[6] Horton D.N.L. and Crolla D.A. Theoretical analysis of the steering behaviour of articulated frame steer vehicles. *Vehicle System Dynamics*, vol. 15, pp. 211—234. 1986.

[7] Merritt, H.E. *Hydraulic Control Systems*. John Wileys and Sons, Cincinnati, Ohio. 1967

[8] Milliken, W.F. and Milliken, D.L. *Race Car Vehicle Dynamics*. SAE International. 1995.

[9] Rahmfeld, R. Development and Control of Energy Saving Hydraulic Servo Drives for Mobile Systems. *Ph.D. Thesis. Dept. of Aircraft Systems, Technical University of Hamburg-Harburg*. Hamburg, Germany. 2002.

[10] Rahmfeld, R. and Ivantysynova, M. Energy Saving Hydraulic Actuators for Mobile Machines. *Proceedings of 1st Bratislavian Fluid Power Sysmposium*, pp. 47-57. Častá – Píla, Slovakia. 1998

[11] Rahmfeld, R. and Ivantysynova, M. Displacement Controlled Wheel Loader – a simple and clever Solution. *4th International Fluid Power Conference Proceedings*, pp. 183-196. Dresden, Germany. 2004.

[12] Williamson, C., Zimmerman, J., and Ivantysynova, M. Efficiency Study of an Excavator Hydraulic System Based on Displacement-Controlled Actuators. *ASME/Bath Workshop on Fluid Power and Motion Control (FPMC08).* Bath, UK. 2008.

[13] Williamson, C and Ivantysynova, M. Power Optimization for Multi-Actuator Pump-Controlled Systems. *Proceedings of the 7th International Fluid Power Conference Aachen 2010 (7IFK)*, Vol 1. pp.91 - 102. 2010.

[14] Wittren, R.A. Power Steering For Agricultural Tractors. *American Society of Agricultural Engineers, Winter Meeting Distinguished Lecture Series*. Chicago, IL, USA. 1975.